A Proposed Mechanism of the Influence of Gold Nanoparticles on DNA Hybridization

Abootaleb Sedighi, Paul C. H. Li,* Idah C. Pekcevik, and Byron D. Gates

Department of Chemistry, Simon Fraser University, Burnaby, British Columbia V5A 1S6, Canada. The manuscript was written through contributions of all authors. All authors have given approval to the final version of the manuscript.

ABSTRACT A combination of gold nanoparticles (AuNPs) and nucleic acids has been used in biosensing applications. However, there is a poor fundamental understanding of how gold nanoparticle surfaces influence the DNA hybridization process. Here, we measured the rate constants of the hybridization and dehybridization of DNA on gold nanoparticle surfaces to enable the determination of activation parameters using transition state theory. We show that the target bases need to be detached from the gold nanoparticle surfaces before zipping. This causes a shift of the rate-limiting step of hybridization to the mismatch-sensitive zipping step. Furthermore, our results propose that the binding of gold nanoparticles to the single-stranded DNA segments (commonly known as bubbles) in the duplex DNA stabilizes the bubbles and accelerates the dehybridization process. We employ the proposed mechanism of DNA hybridization/dehybridization to explain the ability of 5 nm diameter gold nanoparticles to help discriminate between single base-pair mismatched DNA molecules when performed in a NanoBioArray chip. The mechanistic insight into the DNA–gold nanoparticle hybridization/dehybridization process should lead to the development of new biosensors.

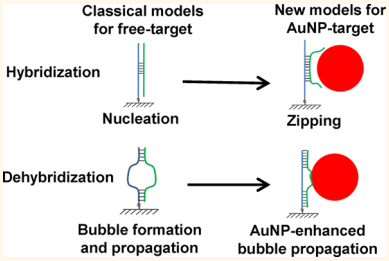

KEYWORDS: DNA hybridization and dehybridization · gold nanoparticle (AuNP) · single base-pair discrimination · NanoBioArray (NBA) chip · Langmuir model · transition state theory · surface plasmon resonance (SPR) spectroscopy

Since the first introduction of gold nanoparticle (AuNP)-based DNA biosensors by the Mirkin group in 1997,[1] there have been numerous other studies reported on DNA biosensors utilizing AuNPs.[2−8] Most applications in DNA biosensing that utilize AuNPs employ the chemisorption of thiol-modified oligonucleotides onto the surfaces of these particles.[9] However, more recent studies have also utilized the adsorption of nonthiolated DNA onto AuNP surfaces.[10] In 2004, Li and Rothberg reported that although double-stranded DNAs (dsDNAs) do not specifically interact with the surfaces of AuNPs without a thiol modification, single-stranded DNAs (ssDNA) can adsorb onto AuNPs.[10,11] Although the nature of adsorption of nonthiolated ssDNA onto the surfaces of AuNPs, both of which are negatively charged, still remains controversial,[10−15] AuNPs loaded with nonthiolated ssDNA have been widely used in a variety of biosensing or diagnostic applications.[10,11,15−23] In most of these applications, ssDNA is adsorbed onto AuNPs due to noncovalent interactions, and a change in the signal (*e.g.*, colorimetric, fluorescence) can result from the close proximity between AuNPs released upon DNA hybridization with complementary ssDNA.[15−21] Previous work by Li *et al.* demonstrated the use of binding of DNA to AuNPs for applications in which the AuNPs were used to hold onto the ssDNA as a cargo in assisting single base pair discrimination,[24,25] but the mechanism of this discrimination is yet to be determined (*vide infra*).

Despite the valuable functionalities of AuNP-loaded ssDNAs in DNA biosensors, there is little information available in the literature about how the presence of AuNPs affects the mechanistic pathway of the hybridization of their DNA cargo.[10−15] For instance, Wu *et al.* observed that a time-dependent dynamic equilibrium exists between the solution-phase hybridized DNAs and the AuNP-loaded ssDNA strands, but the detailed mechanism behind this equilibrium was not clear.[26] It can be implied from the research of several others that

* Address correspondence to paulli@sfu.ca.

Received for review February 9, 2014 and accepted June 25, 2014.

Published online June 25, 2014
10.1021/nn500790m

AuNP binding impacts the kinetics of DNA hybridization.[15,17,18] For example, Ray reported that the hybridization of longer oligonucleotides with their complementary strands (of a fixed size) while loaded onto AuNPs occurred more slowly than the hybridization of shorter oligonucleotides.[18] This observation suggests the involvement of AuNPs in the rate-limiting step of duplex formation since longer oligonucleotides have a higher binding affinity to the AuNP surfaces.[13] However, no experiment has been performed to confirm this hypothesis. Other studies have suggested that AuNPs are involved in the dehybridization of dsDNAs,[27−32] but to the best of our knowledge no experiments have confirmed this hypothesis either. For instance, Cho *et al.* observed that AuNPs enhanced the dehybridization of single base-pair mismatched duplexes,[27] but they did not explain the reason for this observation. In 2009, Chen *et al.* studied the kinetics and thermodynamics of DNA hybridization on the surface of AuNPs, but their findings also did not explain why dehybridization of mismatched duplexes occurred to a greater extent than that observed for perfectly matched duplexes.[33] More surprisingly, Yang *et al.* observed that dehybridization was enhanced even for perfectly matched duplexes in the presence of 5 nm diameter AuNPs, and speculated that the duplex was first adsorbed and then denatured on the surfaces of the AuNPs.[29] This and other studies suggest a discrepancy of how dsDNA binds to the AuNPs,[29,31,32] which is contrary to many other reports concluding that dsDNA does not bind to the AuNPs.[10−13]

Through further research, Li *et al.* have determined that AuNP-loaded DNA targets (AuNP targets), in contrast to the DNA targets freely dissolved in the buffer solution (free targets), were able to discriminate between the perfectly matched immobilized probe from the single base-pair mismatched probes when unaided by thermal stringency at room temperature.[24,25] We hypothesized that AuNPs compete with the immobilized probes to gain the target binding, which increases the stringency of the hybridization process. During this competitive process the mismatched duplex formation with a lower hybridization affinity would be influenced more strongly by the presence of AuNPs than the formation of perfectly matched duplex. The different energy barrier for each of these two processes would enhance the discrimination efficiency between the hybridization of mismatched and perfectly matched duplexes. Utilizing this influence of the AuNPs on discrimination during hybridization, Sedighi *et al.* developed a NanoBioArray chip to detect single nucleotide polymorphisms in the Kras gene codon 12 at room temperature.[25] Room-temperature detection of single nucleotide polymorphisms provides a convenient method for multiplexing in a microarray platform and alleviates the need for temperature optimization during multiple hybridization processes. The mechanism of the observed discrimination is, however, still unknown.

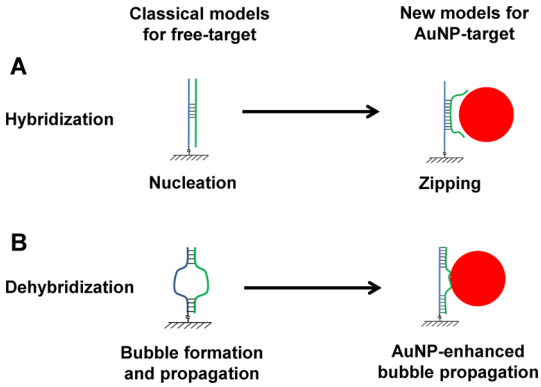

Figure 1. Two models of DNA hybridization and dehybridization. (A) The classical model with the rate-limiting step during hybridization in the free targets, which is altered for the AuNP targets. (B) The stabilization of the naturally formed bubbles by AuNPs modifies the rate-limiting step of dehybridization of double-stranded DNAs and, thereby, accelerates this process.

Here, we aim to study the kinetics for DNA hybridization and dehybridization of AuNP targets and surface-immobilized oligonucleotide probes. These studies are performed using surface plasmon resonance (SPR) spectroscopy, which has the advantage of not requiring target labeling, in order to monitor the hybridization/dehybridization processes. The kinetic rate constants for hybridization to surface bound DNA, determined using SPR, were used to calculate the activation parameters in accordance with transition state theory. New models are proposed herein to describe the influence of gold surfaces on DNA hybridization and dehybridization processes for AuNP targets. These models were based on comparisons between the calculated activation barriers of AuNP targets and the corresponding values resulting from free target processes. Experimental data obtained from this study (*vide infra*) indicates that the rate-limiting step of hybridization is altered from the nucleation step for free targets to the zipping step in AuNP targets (Figure 1A). This study also suggests that AuNPs bind to single-stranded segments (bubbles) as they naturally form during DNA dehybridization, which could accelerate the dehybridization process (Figure 1B). A model for DNA hybridization that takes place within the channels of a NanoBioArray chip was created to better understand the hybridization behavior of AuNP targets within the chip. The results of this study explain observations of AuNP-assisted discrimination during hybridization/dehybridization within the chip, which could be useful in further optimizing this method. These findings address inconsistencies between reports in the literature regarding the impact of AuNP binding on the behavior of DNA hybridization.

RESULTS AND DISCUSSION

The kinetic rate constants for the hybridization of target oligonucleotides to surface-immobilized 20-mer

probes were determined using BIAevaluation software from SPR sensograms obtained using the kinetic titration method. This approach was preferred to the classical method, as the kinetic titration method is faster and requires less amounts of reagents without compromising accuracy of the results.[34] The SPR sensogram in Figure 2 was obtained from the hybridization of a free target strand D20 and its immobilized perfectly matched probe. The sequence information for these DNA strands is reported in Table S1 (Supporting Information). Other SPR sensograms from the kinetic titration analysis of different target oligonucleotides with their perfectly matched and mismatched probes are also shown in Figure S1 (Supporting Information). During these experiments, 10−160 nM of the target oligonucleotides were either free in solution, or loaded on the surfaces of AuNPs and suspended in solution (20 nM). As the concentrations

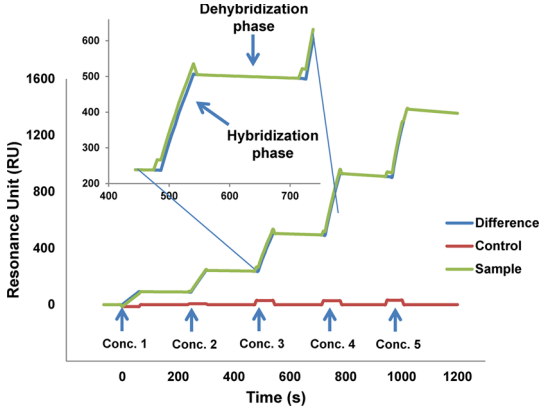

Figure 2. Sensogram resulting from the kinetic titration analysis of 5 different concentrations of free target (D20) analyzed using a SPR sensor chip with D probes (20-mer) immobilized on its surfaces. Concentrations 1−5 represent hybridization−dehybridization experiments conducted for 5 different target concentrations (10−160 nM). The control signal (red) is created as the target solution flows over a region of the sensor surface without immobilized probe molecules. The control signal is subtracted from the sample signal (green) to create the difference signal (blue) that is used for data analysis. The inset depicts the hybridization and dehybridization phases of DNA at 40 nM (concentration 3).

of DNA target molecules in the AuNP target solutions increase from 10 to 160 nM the DNA-to-AuNP ratios also increased from 0.5 to 8.0. A concern with the higher DNA-to-AuNP ratios is that a fraction of the target molecules (in the AuNP target solutions) would remain free in the solution.[13] The excess of target molecules causes the measured values of hybridization rate constants (k_h) for the AuNP targets to have a bias toward values corresponding to the free target.[35] Further analysis (Figure S2, Supporting Information) of the raw data extracted from the sensograms using the method developed by Gotoh *et al.*[36] demonstrated that such a bias did exist at a concentration of 160 nM or a DNA-to-AuNP ratio of 8.0 for both 20-mer and 60-mer targets. The observed bias was more severe for the 60-mer targets because it is harder for the longer oligonucleotides to bind onto the AuNP surfaces at higher DNA target concentrations. Therefore, we chose to omit data from the hybridization using 160 nM of target solutions for calculation of k_h values for both free targets and AuNP targets.

Transition state theory[37] was used to extract mechanistic information from the kinetic parameters. According to this theory, the rate-limiting step of reactions is the formation of the activated complex or transition state.[37] The free energy change of transition state formation ($\Delta G^{\ddagger}$), also known as activation free energy change, is related to the rate constant of the reaction (k) by the Eyring−Polanyi equation, eq 1:

$$k = \frac{k_B T}{h} e^{-\Delta G^{\ddagger}/RT} \quad (1)$$

where k_B is Boltzmann constant, T is absolute temperature, R is universal gas constant and h is Planck constant. Since $\Delta G^{\ddagger}$ includes both the activation enthalpy change ($\Delta H^{\ddagger}$) and the activation entropy change ($\Delta S^{\ddagger}$) and these parameters are related to each other by the equation $\Delta G^{\ddagger} = \Delta H^{\ddagger} - T\Delta S^{\ddagger}$, determination of the rate-limiting step of the reaction using $\Delta G^{\ddagger}$ is superior to using only activation enthalpy changes or $\Delta H^{\ddagger}$.

The k_h values determined from the SPR sensograms (Figure S1, Supporting Information)[34] are reported in

TABLE 1. Kinetic Parameter (k_h) and Activation Parameter ($\Delta G_h^{\ddagger}$) of Hybridization with or without AuNPs (5 nm Diameter) at 22 °C

			free target[b]			AuNP target[b]		
		T_m[a] (°C)	$k_h/10^4$ M^{-1} s^{-1}	$\Delta G_h^{\ddagger}$ kcal/mol	$\Delta\Delta G_h^{\ddagger}$[c] kcal/mol	$k_h/10^4$ M^{-1} s^{-1}	$\Delta G_h^{\ddagger}$ kcal/mol	$\Delta\Delta G_h^{\ddagger}$[c] kcal/mol
W20	PM	57.3	4.22 ± 0.08[b]	11.02 ± 0.01	0.01 ± 0.02	2.03 ± 0.07	11.45 ± 0.02	0.24 ± 0.08
	MM	55.2	4.12 ± 0.12	11.03 ± 0.02		1.35 ± 0.22	11.69 ± 0.08	
D20	PM	56.0	4.34 ± 0.03	10.99 ± 0.01	0.01 ± 0.02	2.01 ± 0.21	11.45 ± 0.05	0.29 ± 0.07
	MM	52.5	4.29 ± 0.18	11.00 ± 0.02		1.22 ± 0.11	11.74 ± 0.04	
D60	PM	56.3	4.38 ± 0.09	11.00 ± 0.02	0.01 ± 0.04	1.42 ± 0.12	11.65 ± 0.04	0.29 ± 0.11
	MM	53.0	4.27 ± 0.17	11.01 ± 0.04		0.94 ± 0.22	11.90 ± 0.10	

[a] Melting temperature as determined by UV absorbance spectroscopy. [b] All standard errors are determined from two measurements, and each include four different target concentrations of 10, 20, 40, and 80 nM. [c] $\Delta\Delta G_h^{\ddagger}$ is the difference between $\Delta G_h^{\ddagger}$ of perfectly matched (PM) and that of mismatched sequences (PM).

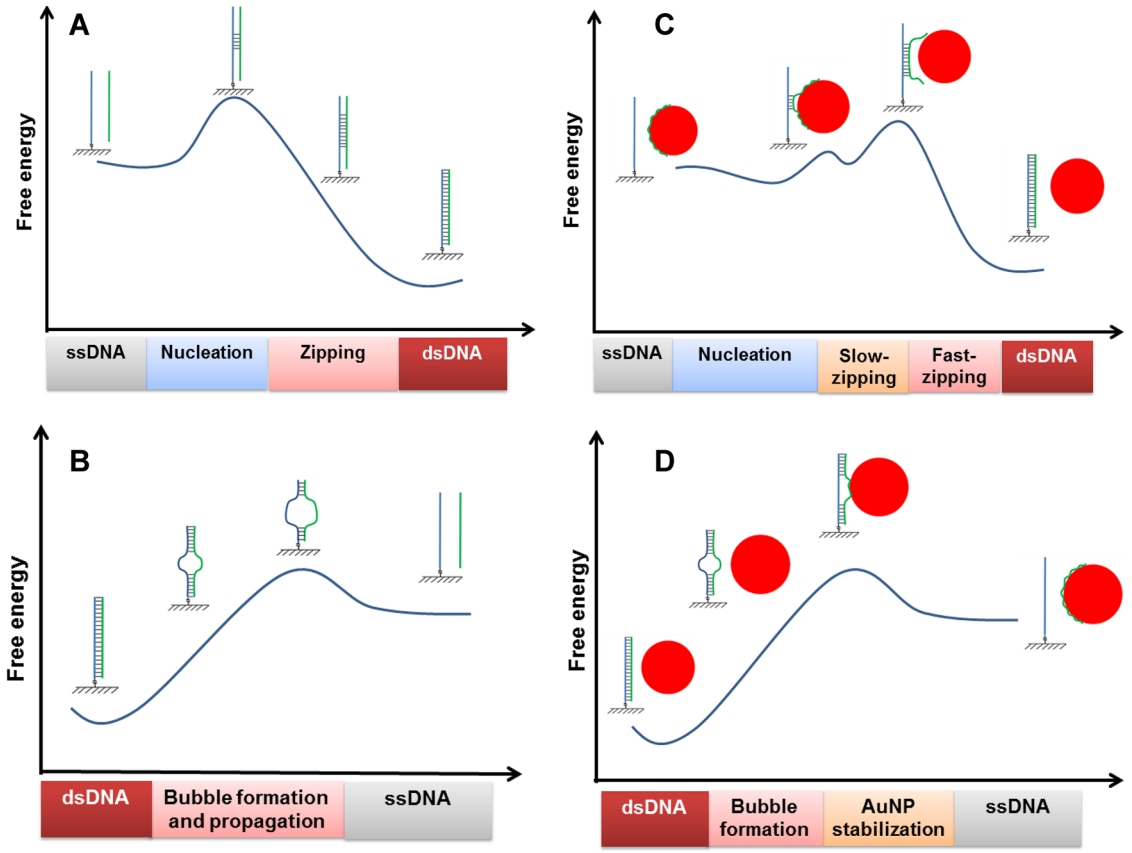

Figure 3. Schematics of classical hybridization (A) and dehybridization (B) models for free targets, and newly proposed models indicating the modifications due to the presence of AuNP targets (C and D, respectively).

Table 1 along with the calculated activation free energy changes. The similar values of k_h for the free target hybridization resulted in the corresponding $\Delta G_h^{\ddagger}$ values to be approximately the same, *i.e.*, ~11 kcal/mol. Therefore, the $\Delta\Delta G_h^{\ddagger}$ values between the perfectly matched duplexes and mismatched duplexes (with a mismatched base-pair at the center of the sequence) are very small, indicating an insensitivity of $\Delta G_h^{\ddagger}$ to the presence of the mismatch site. This mismatch insensitivity of $\Delta G_h^{\ddagger}$ suggests that the mismatched nucleotide does not significantly influence the transition state. This observation agrees with previous reports that the rate-limiting step of free target hybridization is the nucleation step, which is the formation of a few base pairs from each strand into a transient intermediate, called the nucleus.[38] The nucleus usually forms at various sites of the duplex,[39] but the mismatch bases do not take part in the nucleation process.[40] The mismatch bases are incorporated into the duplex during the subsequent zipping process. The zipping is a relatively fast step that occurs subsequent to the rate-limiting nucleation process, and thus the presence of the mismatch base has little influence on the hybridization rate.

On the other hand, AuNP-loaded DNA targets exhibit smaller k_h values, leading to higher $\Delta G_h^{\ddagger}$ in comparison to hybridization with free targets (see Table 1). More noticeably, the k_h values are even lower for the mismatched duplexes, which lead to significantly higher $\Delta\Delta G_h^{\ddagger}$ values in contrast to those for the free targets. In light of these observations, we propose a model for the hybridization of AuNP targets (Figure 3A). We infer that significant differences in $\Delta G_h^{\ddagger}$ originate from a shift in the rate-limiting step from a mismatch-insensitive nucleation step to a mismatch-sensitive zipping step. This shift is, in turn, due to a difference in hybridization environment for AuNP target nucleotides during the zipping step in comparison to the free target nucleotides. Following the nucleation step, the unpaired bases in free targets are free in the solution and hybridize readily due to the negative enthalpy change of base-pair formation.[38] The unpaired bases involved in the zipping step for the AuNP targets have to overcome the potential barriers associated with disrupting the interactions between the bases and the surfaces of the AuNPs. This additional energy barrier hinders the zipping step, making it the rate-limiting step in the hybridization process. The zipping is less favorable in the presence of mismatched bases and results in a higher $\Delta G_h^{\ddagger}$ for hybridization of mismatched duplexes than for perfectly matched duplexes. The zipping step remains slow until binding of the target nucleotides to the AuNPs becomes unfavorable and the target completely detaches from

TABLE 2. Kinetic Parameter (k_d) and Activation Parameter ($\Delta G_d^{\ddagger}$) of Dehybridization with or without AuNPs (5 nm Diameter) at 22 °C

			free target[b]			AuNP target[b]		
		T_m[a] (°C)	$k_d/10^{-4}$ s^{-1}	$\Delta G_d^{\ddagger}$ kcal/mol	$\Delta\Delta G_d^{\ddagger}$[c] kcal/mol	$k_d/10^{-4}$ s^{-1}	$\Delta G_d^{\ddagger}$ kcal/mol	$\Delta\Delta G_d^{\ddagger}$[c] kcal/mol
W20	PM	57.3	1.20 ± 0.02[b]	22.53 ± 0.02	−0.42 ± 0.04	3.18 ± 0.08	21.96 ± 0.03	−0.55 ± 0.09
	MM	55.2	2.46 ± 0.04	22.11 ± 0.02		8.13 ± 0.35	21.41 ± 0.04	
D20	PM	56.0	1.25 ± 0.03	22.51 ± 0.02	−0.64 ± 0.07	3.63 ± 0.14	21.88 ± 0.04	−0.83 ± 0.08
	MM	52.5	3.72 ± 0.11	21.87 ± 0.03		14.9 ± 0.37	21.06 ± 0.02	
D60	PM	56.3	1.21 ± 0.04	22.53 ± 0.03	−0.68 ± 0.07	3.26 ± 0.09	21.95 ± 0.03	−0.95 ± 0.07
	MM	53.0	3.87 ± 0.09	21.84 ± 0.02		16.5 ± 0.44	21.00 ± 0.03	

[a] Melting temperature as determined by UV absorbance spectroscopy. [b] All standard errors are determined from two measurements, and each include five different target concentrations of 10, 20, 40, 80, and 160 nM. [c] $\Delta\Delta G_d^{\ddagger}$ is the difference between $\Delta G_d^{\ddagger}$ of perfectly matched (PM) and that of mismatched (MM) sequences.

the surfaces of the AuNPs. Once detached from the AuNPs, the remaining bases will hybridize at a faster rate to complete the zipping step. This process of detachment in the zipping step should be even slower for longer targets due to the increased number of interactions with the surfaces of the AuNPs (see the investigation on the effect of target length in the subsequent section).

We also investigated the influence of the type of mismatched base-pair on the hybridization reaction kinetics. For example, the mismatched site of the W20 duplex comprises a G−T base-pair, which is among the least unstable mismatches, and the mismatched duplex of the D20 contains the more unstable C−A mismatch.[41] This is consistent with our measurement of various melting temperatures, which determined the lowest melting temperature for the D20 mismatched base pair (Table 1). However, based on the similar $\Delta\Delta G_h^{\ddagger}$ values for both the W20 and D20 AuNP targets (Table 1), we speculated that although the mismatch will influence the hybridization process the type of the mismatch is not critical. The type of mismatch would have a greater influence on the melting temperatures during dehybridization processes and will be discussed in the following paragraph.

Table 2 shows the dehybridization constants as well as the corresponding changes in activation free energy. The rate-limiting step in the dehybridization of dsDNA is the formation of single-stranded segments (referred to as bubbles) at different sites along the duplex (Figure 3A). These bubbles form due to the continuous cycle between local denaturation and reclosing, known as thermal breathing of dsDNA.[42] The presence of a mismatched base-pair in the duplex strand accelerates the formation of bubbles. Unlike the hybridization rate constants, k_h, the dehybridization rate constants, k_d, are highly influenced by the presence of mismatched base-pairs.[43] Furthermore, variations in the stabilities of mismatches contribute to differences observed in the rate of formation of bubbles.[43] These differences are reflected in the variations in k_d values of free target duplexes shown in Table 2, in contrast to having similar k_h values (Table 1). Regarding the mismatch types, C−A mismatches in the D20 duplex are more unstable, which results in their k_d value being ∼3 times higher for the mismatched base-pairs than that for the perfectly matched duplex. This result is in contrast to the ∼2 times increase observed in the case of the most stable W20 duplex. Moreover, the higher k_d value of D20 leads to a more negative $\Delta\Delta G_d^{\ddagger}$ of −0.64 kcal/mol than the corresponding value of W20 (−0.42 kcal/mol).

Even higher dehybridization rates were observed for AuNP targets with both perfectly matched and mismatched probes. In the case of perfectly matched duplexes, the k_d values increased from $\sim 1 \times 10^{-4}$ s^{-1} observed for the free targets to $\sim 3 \times 10^{-4}$ s^{-1} in AuNP targets. These results suggest a greater role of AuNPs in the DNA dehybridization process than during hybridization. In the case of mismatched duplexes using AuNP targets, the increase in k_d was ∼3 times for the G−T mismatch and ∼4 times for the C−A mismatch, corresponding to the relative instability of these duplexes. In the case of D20 for the C−A mismatch, a 4-fold increase of k_d for mismatched over perfectly matched is the integral to further understanding the mechanism of AuNP-assisted single base-pair discrimination. In the case of the AuNP-W20 target, the combination of the $\Delta\Delta G_d^{\ddagger}$ value (−0.55 kcal/mol) with the $\Delta\Delta G_h^{\ddagger}$ value (0.24 kcal/mol) suggest a better discrimination of AuNP-W20 targets over the free W20 targets ($\Delta\Delta G_d^{\ddagger}$ of −0.42 kcal/mol and $\Delta\Delta G_h^{\ddagger}$ of 0.01 kcal/mol). Moreover, the greater influence of AuNPs on the dehybridization process than hybridization suggests that the discrimination is better for D20 ($\Delta\Delta G_d^{\ddagger}$ of −0.83 and $\Delta\Delta G_h^{\ddagger}$ of 0.29 kcal/mol) in comparison to W20 ($\Delta\Delta G_d^{\ddagger}$ of −0.55 and $\Delta\Delta G_h^{\ddagger}$ of 0.24 kcal/mol).

Since the binding of AuNPs to the bases is rather nonspecific, acceleration of the dehybridization process by AuNP binding is expected to be independent of the mismatch base-pair stability. Furthermore, AuNPs have been frequently reported to not bind with dsDNA.[10−18] We can explain the correlation between our results and these previous reports by revisiting the

TABLE 3. Kinetic Parameters (k_h, k_d) and Activation Parameters ($\Delta G_h^{\ddagger}$, $\Delta G_d^{\ddagger}$) of AuNP Targets for AuNPs of Two Different Sizes and for Free Targets Hybridized to, and Dehybridized from 20-mer DNA Probes at 22 °C

	free target			AuNP (5 nm diameter) target			AuNP (12 nm diameter) target		
hybridization	$k_h/10^4$ M^{-1} s^{-1}	$\Delta G_h^{\ddagger a}$ kcal/mol	$\Delta\Delta G_h^{\ddagger}$ kcal/mol	$k_h/10^4$ M^{-1} s^{-1}	$\Delta G_h^{\ddagger}$ kcal/mol	$\Delta\Delta G_h^{\ddagger}$ kcal/mol	$k_h/10^4$ M^{-1} s^{-1}	$\Delta G_h^{\ddagger}$ kcal/mol	$\Delta\Delta G_h^{\ddagger}$ kcal/mol
PM	4.34 ± 0.03[b]	10.99 ± 0.01	0.01 ± 0.02	2.01 ± 0.21	11.45 ± 0.05	0.29 ± 0.07	2.08 ± 0.14	11.43 ± 0.04	0.27 ± 0.09
MM	4.29 ± 0.18	11.00 ± 0.02		1.22 ± 0.11	11.74 ± 0.04		1.31 ± 0.23	11.70 ± 0.08	
dehybridization	$k_d/10^{-4}$ s^{-1}	$\Delta G_d^{\ddagger a}$ kcal/mol	$\Delta\Delta G_d^{\ddagger}$ kcal/mol	$k_d/10^{-4}$ s^{-1}	$\Delta G_d^{\ddagger}$ kcal/mol	$\Delta\Delta G_d^{\ddagger}$ kcal/mol	$k_d/10^{-4}$ s^{-1}	$\Delta G_d^{\ddagger}$ kcal/mol	$\Delta\Delta G_d^{\ddagger}$ kcal/mol
PM	1.25 ± 0.03[c]	22.51 ± 0.02	−0.64 ± 0.07	3.63 ± 0.14	21.88 ± 0.04	−0.83 ± 0.08	1.17 ± 0.07	22.55 ± 0.06	−0.65 ± 0.11
MM	3.72 ± 0.11	21.87 ± 0.03		14.9 ± 0.37	21.06 ± 0.02		3.57 ± 0.11	21.89 ± 0.03	

[a] $\Delta G_h^{\ddagger}$ and $\Delta G_d^{\ddagger}$ are activation free energy changes for hybridization and dehybridization, respectively; $\Delta\Delta G_h^{\ddagger}$ is $\Delta G_h^{\ddagger}$ of perfectly matched (PM) minus that of mismatched (MM), and $\Delta\Delta G_d^{\ddagger}$ is $\Delta G_d^{\ddagger}$ of PM minus that of MM. [b] All standard errors for k_h values are determined from two measurements, and each include 4 different target 20-mer DNA concentrations of 10, 20, 40 and 80 nM. [c] All standard errors for k_d values are determined from two measurements, and each include 5 different 20-mer target DNA concentrations of 10, 20, 40, 80 and 160 nM.

rate-limiting step of the dehybridization process for AuNP targets. Figure 3B shows a potential AuNP-mediated dehybridization process (in AuNP targets), in which ssDNA bubbles are formed, in a manner similar to natural dehybridization (in free targets). Although fully coiled duplex DNAs do not bind to AuNPs, once the ssDNA bubbles form they are able to bind to the AuNPs. Therefore, the energy released from the interactions between the dehybridized bases and surfaces of the AuNPs may compensate for the energy required for the remaining bases to undergo dehybridization from the probe molecules, thus accelerating the process of duplex dehybridization. Our model suggests that dehybridization in the experiment by Yang *et al.*[28] was actually initiated by binding of the AuNPs with the thermal bubbles (or ssDNA segments in the duplex), but not to the fully coiled dsDNA.[28] Other biological events have also been reported to involve binding with thermally formed bubbles. For example, TATA binding protein (TBP), a transcription promoter, binds to bubbles of DNA that form by thermal breathing.[44]

Effect of Target Length. Longer oligonucleotides are known to bind more tightly to the AuNP surfaces,[14] most likely due to the potentially higher number of contact points between the oligonucleotides and the surfaces of the AuNPs. In order to investigate the influence of target length, and thus AuNP binding strength, on the hybridization and dehybridization processes, we performed SPR studies using targets of two different lengths. These targets were D60 (60-mer) and D20 (20-mer) (see Table S1, Supporting Information). The measured hybridization rate constants and the corresponding activation parameters of D60 are shown in Table 1. In comparison to the D20 targets conjugated to 5 nm diameter AuNPs, D60 shows slower reaction rates (*i.e.*, 1.42 *vs* 2.01 × 10^4 M^{-1} s^{-1}) indicating a higher energy barrier for hybridization. In accordance with our proposed model of AuNP target hybridization, we believe that for longer target molecules, due to the greater number of contact points with the AuNP surfaces, the slow-zipping step (the rate-limiting step) lasts longer, and consequently the hybridization rate is reduced due to the greater number of contact points with the gold surfaces. Unlike the differences observed in the hybridization rates, the D60 target had similar dehybridization rates in comparison to the D20 targets (3.26 *vs* 3.63 × 10^{-4} s^{-1}, respectively), which suggests binding between the AuNPs and the dangling region of the D60 target does not enhance its dehybridization.

Effect of AuNP Size. The ssDNAs have been observed to bind less tightly to small AuNPs in comparison to larger AuNPs.[14,45] A higher degree of curvature in the smaller AuNPs appears to have an adverse effect on binding strength. In order to investigate the influence of AuNP size on interaction with the oligonucleotides, we measured the kinetic rate constants of D20 targets loaded onto 12 nm diameter AuNPs and compared their hybridization and dehybridization parameters with the corresponding values for D20 loaded onto 5 nm diameter AuNPs. Both values were also compared with those obtained for free targets. From the derived k_h values (Table 3) it can be observed that the 12 nm AuNP targets had a similar hybridization rate to that of the 5 nm AuNP targets (*i.e.*, 2.08 *vs* 2.01 × 10^4 M^{-1} s^{-1}, respectively). The values of $\Delta\Delta G_h^{\ddagger}$ for the perfectly matched and mismatched probes remain similar between the 5 nm AuNP (0.29 kcal/mol) and 12 nm AuNP (0.27 kcal/mol).

On the other hand, the rates of dehybridization for the duplexes were not increased in the presence of 12 nm AuNP and the k_d values were similar to those for the free targets (1.17 *vs* 1.25 × 10^{-4} s^{-1}, respectively). This result is in contrast to the values observed for 5 nm AuNP and for free targets (3.63 × 10^{-4} *vs* 1.25 × 10^{-4} s^{-1}), as shown in Table 3. These observations suggest that the 12 nm AuNP is not significantly involved in the dehybridization process in contrast to 5 nm AuNP. While the k_h values indicate similar binding strength between the DNA bases and surfaces

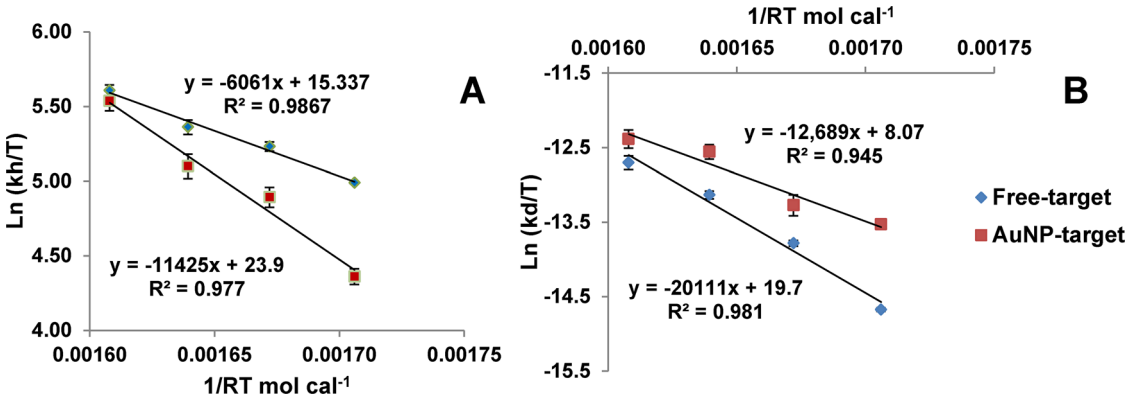

Figure 4. Arrhenius plots of hybridization rate constants (A) and dehybridization rate constants (B) at temperatures of 40, 34, 28, and 22 °C.

of AuNPs with different sizes, one may anticipate a similar dehybridization rate for the 12 nm AuNPs. The apparent decreased involvement in the dehybridization process by the larger AuNPs might be due to their relatively smaller degree of curvature. The surfaces of the citrate-capped AuNPs are negatively charged. However, the dsDNA regions adjacent to the ssDNA segments (bubbles) are also negatively charged (with double charge density in comparison to regions with ssDNA segments), and their electrostatic repulsion prevents the AuNPs from effectively approaching the ssDNA segments. The 5 nm AuNPs have a larger degree of curvature, such that there is less electrostatic repulsion during the dehybridization process.

Extraction of Activation Enthalpy and Entropy Changes. Additional SPR experiments were conducted at 28, 34, 40 °C, and Arrhenius plots were constructed in order to extract the activation enthalpy and entropy changes. A rearranged format of the Eyring–Polanyi equation was used (eq 2) to obtain the contributions of the enthalpy and entropy changes in $\Delta G^{\ddagger}$.

$$k = \frac{k_B T}{h} e^{(-\Delta H^{\ddagger}/RT)} e^{(\Delta S^{\ddagger}/R)} \quad (2)$$

Figure 4 shows the Arrhenius plot (ln k_h/T *versus* $1/RT$) of hybridization rate constants (Figure 4A) and dehybridization rate constants (Figure 4B) for D20 in the range of 22 to 40 °C. The activation enthalpy change ($\Delta H^{\ddagger}$) and activation entropy change ($\Delta S^{\ddagger}$) were derived (Table 4) from the slope and intercept of the Arrhenius plots and using eq 2 (see Table S2, Supporting Information).[32] In agreement with previous reports,[43,46] the k_h values of the free targets almost doubled with the temperature increased from 22 to 40 °C. This results in a positive $\Delta H^{\ddagger}$ (Table 4), which has been previously suggested to correlate with diffusion-controlled nucleation process.[38,42,47] 5 nm AuNP targets, on the other hand, demonstrate a sharper increase in the k_h values (*i.e.*, a more negative slope), which approach the values of the free targets at 40 °C (*i.e.*, $1/RT$ = 0.0016 M K cal^{-1}). This results in a doubling of $\Delta H_h^{\ddagger}$ in comparison to the free targets, which is consistent with the observed increase of $\Delta G_h^{\ddagger}$ values for the 5 nm AuNP targets.

TABLE 4. Activation Enthalpies and Entropies of Free Targets and 5 nm AuNP Targets

	$\Delta H_h^{\ddagger a}$ kcal mol^{-1}	$\Delta S_h^{\ddagger a}$ cal mol^{-1} K^{-1}	$\Delta H_d^{\ddagger b}$ kcal mol^{-1}	$\Delta S_d^{\ddagger b}$ cal mol^{-1} K^{-1}
free target	6.06 ± 0.50	−16.72 ± 0.83	20.11 ± 1.97	−7.99 ± 3.26
AuNP5 target	11.42 ± 1.24	0.26 ± 2.05	12.69 ± 2.18	−31.14 ± 3.60

[a] Obtained from k_h measurements at four different temperatures of 40, 34, 28, and 22 °C, based on eq S2a of Table S2 (Supporting Information). [b] Obtained from k_d measurements at four different temperatures of 40, 34, 28, and 22 °C, based on eq S2b of Table S2 (Supporting Information).

The negative value of $\Delta S_h^{\ddagger}$ for free targets indicates a drop in the system's disorder in the rate-limiting step as the nucleus forms between the two DNA strands. However, the value of $\Delta S_h^{\ddagger}$ for AuNP targets is positive. Although this value has a high estimated error value, it is clearly less negative than the free target value. We attribute this less negative $\Delta S_h^{\ddagger}$ to the involvement of AuNP binding in the rate-limiting step of hybridization. We believe that during hybridization involving the AuNP target, the entropy loss due to the hydrogen binding between the DNA bases is compensated by the entropy gain arising from the detachment of target bases from the surfaces of the AuNPs. Therefore, a less negative $\Delta S_h^{\ddagger}$ is observed for AuNP target hybridization than the free target hybridization, because the latter only involves the entropy decrease associated with hydrogen binding in its rate-limiting nucleation step.

A reverse trend was observed in the dehybridization parameters. The 5 nm AuNP targets have a lower value for $\Delta H_d^{\ddagger}$ than the free targets because the transition state is stabilized by binding with the AuNPs. A more negative $\Delta S_d^{\ddagger}$ value associated with the AuNP targets demonstrates the hindrance of the transition state and further implicates the involvement of AuNPs in the rate-limiting step.

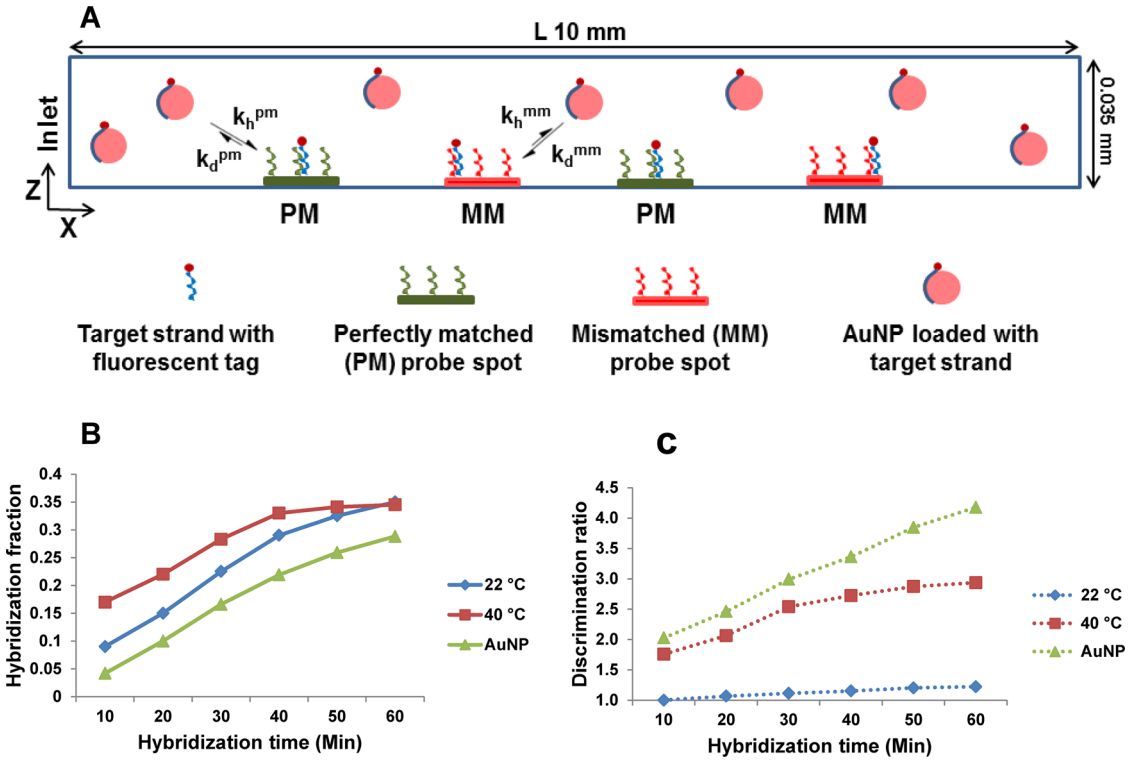

Figure 5. (A) A model of AuNP target hybridization that takes place in the channel of a NanoBioArray chip. Two perfectly matched (PM) probe spots and two mismatched (MM) probe spots are alternately arrayed on the surfaces within the channel. (B) Predicted DNA duplex concentration and (C) predicted discrimination ratios plotted against the time permitted for hybridization that resulted from D20 targets (free targets at 22 and 40 °C, and targets loaded on 5 nm AuNPs at 22 °C). Hybridization fractions are the fractions of PM probes that form duplexes with the targets, and discrimination ratios (dashed lines) are derived from the ratio of PM duplexes to MM duplexes.

DNA Hybridization Model in the NanoBioArray Chip. After better establishing the role of AuNPs in hybridization and dehybridization, we apply this knowledge to estimate the hybridization results for experiments involving NanoBioArray chips for the single nucleotide polymorphisms (SNPs) detection of Kras gene.[25] We created a model of the DNA hybridization processes taking place within the channel of the NanoBioArray chip (Figure 5A). Our goal was to further understand the behavior of the AuNP targets and to further verify the kinetic parameters obtained from the SPR spectroscopy measurements through the use of experimental results obtained from the NanoBioArray chip. As described in the subsequent experimental section, the hybridization fractions (θ^{pm} for perfectly matched duplexes and θ^{mm} for mismatched duplexes) were determined from the knowledge of the diffusion coefficient, D, of the AuNPs (from dynamic light scattering (DLS) measurements) and of the maximum duplex concentration, θ_0 (from the calibration measurements performed using the NanoBioArray chip).

From the DLS experiments the measured hydrodynamic diameter, d_h, values were used to derive D using the Einstein–Stokes equation (eq 5, see experimental section below). The value of d_h for the 5 nm diameter AuNPs (before DNA loading) was determined to be 6.8 (±0.2) nm, which increased to 7.6 (±0.5) nm when loaded with the D20 target. The calculated value of D was 6.4×10^{-7} cm^2/s for the 20-mer AuNP targets, which was about half of the value (1.47×10^{-6} cm^2/s) estimated for the 20-mer free targets. The values for θ_0 were experimentally obtained from both the measurements of SPR and experiments using the NanoBioArray chip. On the basis of the SPR responses before and after probe immobilization, we estimated that the probe density on the surfaces of the SPR sensor chip, as determined by the instrument settings,[48] was $(1.1 \pm 0.3) \times 10^{-8}$ mol/m^2. This value is relatively close to the corresponding value obtained from the experiments using the NanoBioArray chip [$(1.4 \pm 0.2) \times 10^{-8}$ mol/m^2]. Both values of the probe densities are at a low level, which suggests that the probe–probe interactions are minor.[49]

Figure 5B compares the fluorescence signal intensities resulting from the hybridization (indicated by the hybridization fraction) using D20 free targets (at 22 and 40 °C) with those values for 5 nm AuNP-D20 targets at 22 °C measured at various hybridization times. The hybridization fraction, which is θ^{pm} in eq 8 (see experimental section below) divided by θ_0, is a measure of sensitivity for the formation of the perfectly matched duplexes. In a similar manner θ^{mm} in eq 9 (see experimental section below) divided by θ_0 gives the hybridization fraction for the mismatched duplexes. The various conditions are easily compared by plotting

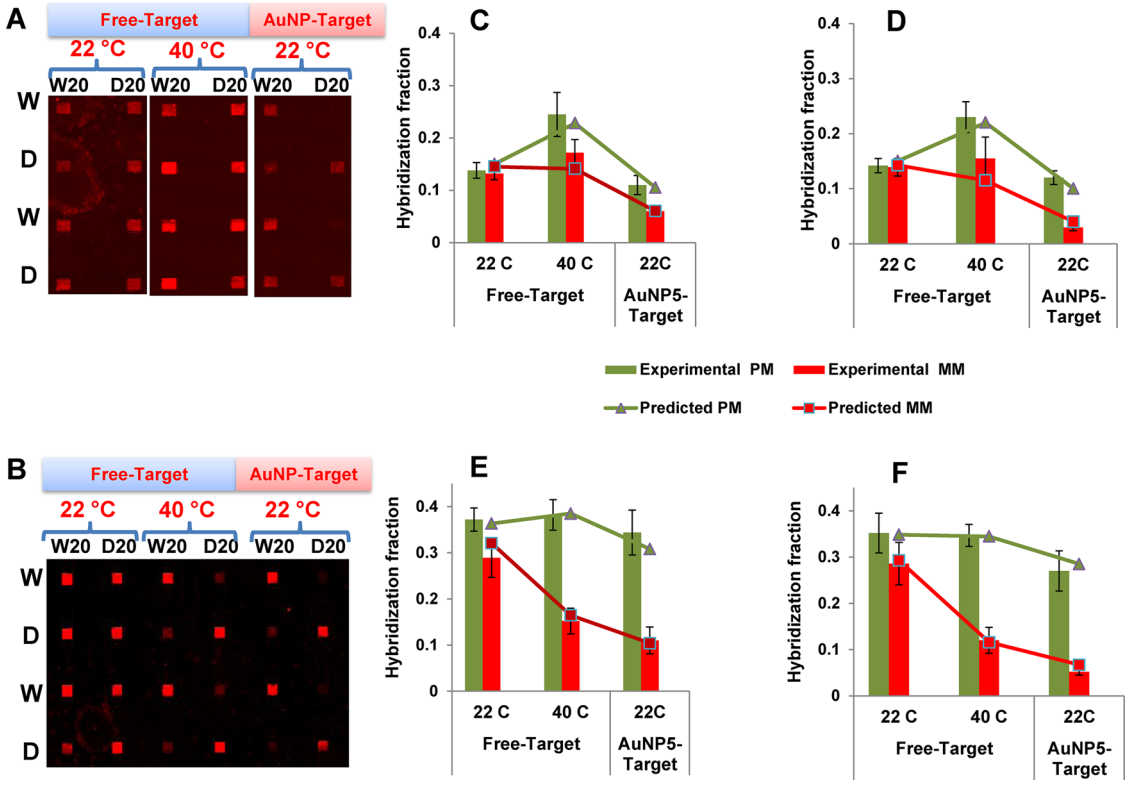

Figure 6. Comparison of predicted and experimentally measured fluorescent intensities from the formation of surface-bound DNA duplexes. Scanned fluorescence images of the NanoBioArray chips contain spots associated with either 20 min (A) or 60 min (B) periods of hybridization. The histograms (C) and (D) correspond to the integrated fluorescence signals from a 20 min hybridization of W20 and D20 targets, respectively, from 10 nM free DNA. Similarly, the histograms in (E) and (F) correspond to analysis of the 60 min hybridization processes for W20 and D20, respectively. Histograms created from experimentally derived fluorescence signal intensities are shown in the columns (background-corrected and averaged between two independent spots) and plotted in comparison to the signals predicted from the hybridization model (lines). In order to convert the measured signal intensities into the "hybridization fraction", a calibration curve of free targets was created from concentrations from 0.1 nM (lowest end of linear range) to 100 nM (at which the measured signal intensity was saturated). Measured fluorescence signal intensities were converted into fractions of the maximum observed fluorescence signal.

the discrimination ratios, which are the fraction of perfectly matched duplexes over the fraction of mismatched duplexes (θ^{pm}/θ^{mm}). In comparison to the hybridization fraction at 40 °C, the free target signals at 22 °C are smaller at short hybridization times (Figure 5B). This difference is primarily attributed to their lower k_h values at 22 °C. At longer hybridization times, however, the intensity of the hybridization fraction at 22 °C became equivalent to that at 40 °C. This time dependence is attributed to a greater influence of the slower dehybridization rates at 22 °C that compete with the relatively slower hybridization process.

Similar trends apply to the AuNP targets, except that they exhibit a relatively lower intensity of the hybridization fraction even after 60 min of hybridization (Figure 5B). The discrimination ratios for the AuNP targets are, on the other hand, higher than those for the free targets at 22 or 40 °C for all hybridization times. This variation in the discrimination ratio is primarily due to the larger differences in the perfectly matched and mismatched dehybridization constants for the AuNP targets, in contrast to the corresponding differences for the free targets (Table 2).

The fluorescence responses predicted by the model were verified by the experimental signals obtained using the NanoBioArray chip at two different hybridization times. As previously reported, hybridization occurred within these microfluidic devices at the intersections between the vertical target DNA channels and the horizontally preprinted (DNA) probe lines.[25] Figure 6A,B shows representative images of the fluorescence signals obtained from the 20 and 60 min hybridization processes, respectively. The histograms (Figures 6C–F) show the experimentally measured hybridization fractions of perfectly matched (in green) and mismatched (in red) duplexes. Histograms in Figure 6C,D correspond to the signal intensities from a 20 min hybridization of W20 (Figure 6C) and D20 (Figure 6D), while the histograms in Figure 6E,F show the corresponding graphs from the 60 min hybridization process. The experimentally derived signals (plotted as columns) are compared with the values predicted by the model (plotted as solid lines). This comparison indicates agreement between the predicted and experimental values within experimental error. This agreement illustrates the accuracy of the

rate constants, as determined from the SPR measurements, used in the model in predicting the experimental results obtained using the NanoBioArray chip.

CONCLUSION

In this study, the influence of binding between gold nanoparticles and DNA molecules during DNA hybridization was investigated in detail. This study compared the hybridization of DNA targets loaded onto the surfaces of AuNPs (AuNP targets) with the hybridization of free DNA targets to surface-bound DNA probes. We measured the kinetic rate constants for the hybridization and dehybridization processes and determined the activation parameters of AuNP-loaded targets in comparison to their equivalent free targets. Our studies suggest a mechanism that the rate-limiting step in the hybridization process is the DNA zipping step in the AuNP targets and that AuNPs enhance the dehybridization of duplexes by stabilization of thermally formed DNA bubbles. The findings of this study provide a mechanism for the observed AuNP-assisted single base-pair discrimination in a NanoBioArray chip. More importantly, the results of this investigation reveal details behind the discrepancy in the literature regarding DNA hybridization using AuNP-loaded DNA strands, which has been widely used in a number of recent biosensors. These results may be utilized to develop novel AuNP-based DNA biosensors in the future.

EXPERIMENTAL SECTION

Materials. Gold nanoparticles (stabilized with citrate and tannic acid) of 5 nm diameter were purchased from Sigma Life Science, and 12 nm diameter gold nanoparticles (capped with citrate) were obtained from NanoComposix (CA, USA). Sodium dodecyl sulfate (SDS), 3-aminopropyltriethoxysilane (APTES), 25% glutaraldehyde, cetyltrimethylammonium bromide (CTAB) and Triton X-100 were purchased from Sigma-Aldrich. Negative photoresist (SU-8 50) and its developer were purchased from MicroChem Corp. (Newton, MA). Glass slides with dimensions of 3 in. $\times$ 2 in. were obtained from Fisher Scientific Co. (Ottawa, ON, Canada).

All the reagents and materials required for surface plasmon resonance (SPR) experiments including 1-ethyl-3-(3-(dimethylamino)propyl) carbodiimide (EDC), *N*-hydroxysuccinimide (NHS), ethanolamine, HBS-N Buffer (0.01 M HEPES pH 7.4, 0.15 M NaCl) and CM5 sensor chips, were provided by GE Healthcare (UK).

All oligonucleotides were synthesized and modified by Integrated DNA Technologies (Coralville, IA). Wild-type (W) and G12D (D) target oligonucleotides (20 or 60 bases long) with the sequence of Kras gene were modified with a biotin molecule at the 5′-end (Table S1, Supporting Information). The sequences were designed in such a way that the codon 12 sequence was located at the center of the oligonucleotides. The 20-mer probe oligonucleotides, with each of them complementary to one of the targets (either W or D), were designed. The probes were modified with an amine group and a C12 spacer at the 5′-end. All oligonucleotides and their sequences are listed in Table S1 (Supporting Information).

Surface Plasmon Resonance (SPR) Spectroscopy. All the SPR measurements were performed on BIAcore X100 (GE Healthcare). Immobilization of the amine-labeled DNA probes on the CM5 sensor chip, mediated by CTAB, was carried out using a company-developed protocol.[50] Briefly, the sensor surface was activated by an EDC/NHS mixture (1:1, v/v), which converted the carboxylic groups to succinimide groups required for amine binding. Then the probe molecules were immobilized on the sensor surface by running the immobilization solution containing the probe molecules (50 μM) and CTAB (0.6 mM) over the sensor surfaces. Finally, unreacted succinimide groups were deactivated using an ethanolamine hydrochloride solution (pH 8.5). Free target solutions were prepared with target concentrations of 10, 20, 40, 80, and 160 nM. The AuNP target solutions were prepared with identical concentrations of the target DNA, but each contained an AuNP concentration of 20 nM. The mixed solutions were incubated thereafter at 95 °C for 5 min and then suspended in HBS-N (containing 0.15 M of NaCl) as the hybridization buffer. The kinetic rate constants of DNA hybridization were determined using the kinetic titration procedure.[34] This method was preferred to the classical method as the analysis is faster and requires less reagents without compromising the accuracy.[34] The target solutions continuously flowed for 30 s on the sensor chip surface (with immobilized probe), starting from the lowest concentration to the highest. Following the hybridization of each target solution, the dehybridization buffer was introduced by a continuous flow over the sensor surface for 60 s. The HBS-N buffer was used as the dehybridization buffer for the free target solution, while the dehybridization buffer for the AuNP targets was HBS-N buffer containing the AuNP loaded with negative control oligonucleotides, with the same target length but an unrelated sequence.

During the course of the experiment the SPR instrument measures the changes in the refractive index within a thin layer above the sensor chip and records changes in resonance units (RU). The resulting SPR sensogram contains a double-phase cycle, and each cycle (experiment run with each concentration) consists of a hybridization phase and a dehybridization phase (Figure 2). During each cycle, the RU value increases as a result of the hybridization to the immobilized probes by the target molecules which were either free or loaded onto surfaces of the AuNPs. The dehybridization phase of the sensogram was generated as the blank solution flowed over the sensor surface following each hybridization phase. The hybridization buffer (the buffer in which the target molecules were dissolved) was used as the blank solution for the free targets. Aiming to investigate the dehybridization process in the presence of AuNPs, the blank solution for the AuNP targets also contained AuNPs loaded with oligonucleotides with unrelated sequences. At the end of the dehybridization phase in the last cycle, the regeneration buffer (50 mM NaOH) was added to remove all the hybridized targets and regenerate the sensor chip surface for subsequent experiments. The BIAevaluation software (GE Healthcare) was used to analyze the sensogram to extract the hybridization and dehybridization rate constants as given by the Langmuir eqs 3 and 4, respectively.[34]

$$\frac{dR}{dt} = k_h C[R_{max} - R] - k_d R \quad (3)$$

$$\frac{dR}{dt} = -k_d R \quad (4)$$

where k_h, C and k_d are the hybridization rate constant, target concentration and the dehybridization rate constant, respectively. The response at each time of the blank sensogram was subtracted from the corresponding sample response to give the subtracted value R. The R values were used to indicate the duplex concentration at each time, and the maximum response (R_{max}) was taken to represent the probe concentration in the Langmuir equation. The rate of duplex formation (dR/dt), acquired by nonlinear fitting of the sensogram, contains both the hybridization and dehybridization terms of the Langmuir equation (eq 3) during the hybridization phase. While in the dehybridization phase, dR/dt only contains the dehybridization

term (eq 4). Therefore, both kinetic rate constants k_h and k_d have been calculated using the sensogram information.

Dynamic Light Scattering (DLS) Measurements. The hydrodynamic diameters of the AuNP targets were measured by dynamic light scattering (DLS) using a Zetasizer Nano instrument (Malvern Instruments, UK). The AuNP solutions (5 nm diameter) were incubated with W20 targets (concentration ratio of 1:1) at 95 °C for 5 min, cooled down to room temperature, and were directly measured by DLS. The same procedure without the addition of W20 targets was followed to measure the hydrodynamic diameter of pristine AuNPs. From the DLS measurements the hydrodynamic diameter (d_h) of the nanoparticle was measured, and the diffusion coefficient D could be derived using the Einstein−Stokes equation, eq 5:[51]

$$d_h = \frac{k_B T}{3\pi\eta D} \tag{5}$$

where k_B is Boltzmann constant, η is dynamic viscosity of the solvent, and T is the temperature in Kelvin.

Melting Temperature Measurement. The UV absorbance spectra of the DNA were recorded using a Cary 300 Bio UV−visible spectrophotometer (Varian). Equal molar concentrations of probes and targets were dispersed in the hybridization buffer (HBS-N) and incubated overnight at room temperature. The absorbance hyperchromicity was recorded by monitoring the absorbance at 260 nm with a linear heating rate of 0.5 °C/min, starting from 25 to 85 °C.

Model for DNA Hybridization in a NanoBioArray Chip Channel. The incompressible Navier−Stokes equation was used to simulate the microfluidic flow in NanoBioArray channels. The channels are long and rigid, in which there is a steady-state laminar flow in the x-direction. In order to simulate the target concentrations along the z- and x-directions, we use two-dimensional geometry (Figure 5A). The incompressible Navier−Stokes equation in these conditions is thus reduced to eq 6:

$$u = 6u_{ave}\frac{z}{h}\left(1 - \frac{z}{h}\right) \tag{6}$$

where u is the flow velocity in each point (z) along the channel's height, u_{ave} is the average flow velocity, and h is the channel height.

Since the target molecules were transported *via* both diffusion as well as convection, the transient two-dimensional mass transport can be described by eq 7:

$$\frac{\partial C}{\partial t} = D\left(\frac{\partial^2 C}{\partial x^2} + \frac{\partial^2 C}{\partial z^2}\right) - u\left(\frac{\partial C}{\partial x}\right) \tag{7}$$

where C represents the target concentration and D is the target diffusion coefficient. Stellwagen *et al.*[52] suggested an empirical equation for the diffusion coefficients of DNA in water: $D = 7.38 \times 10^{-6}$ cm^2/s · [base number]$^{-0.539}$, which was used to calculate the D value of free targets. The D value of the AuNP targets was measured from DLS measurement, as mentioned in the main text. As the target molecules are transported along the channel, they reach the perfectly matched and mismatched probe spots on the channel surfaces where the probe molecules are anchored to these surfaces. It is at these regions that the hybridization process occurs between the target molecules and probe molecules. The rate of the hybridization, between the solution-phase target and the surface-bound probe, is governed by the Langmuir equation and varies between the perfectly matched and mismatched probe spots, as shown in eqs 8 and 9:

$$\frac{\partial \theta^{pm}}{\partial t} = k_h^{pm} C(\theta_0 - \theta^{pm}) - k_d^{pm}\theta^{pm} \tag{8}$$

$$\frac{\partial \theta^{mm}}{\partial t} = k_h^{mm} C(\theta_0 - \theta^{mm}) - k_d^{mm}\theta^{mm} \tag{9}$$

where C represents the target concentration determined by eq 7, θ_0 represents the maximum duplex concentration or total surface probe density, and θ^{pm}, k_h^{pm} and k_d^{pm} are the duplex concentration, hybridization constant and dehybridization constant, respectively, at the perfectly matched probe regions. θ^{mm}, k_h^{mm} and k_d^{mm} are the corresponding values at the mismatched probe regions. In order to estimate the surface probe densities (θ_0) on the NanoBioArray chip, solutions containing fluorescently labeled probes were filled inside the channels, and a calibration graph was established that correlated the observed fluorescence signals to the number of probe molecules per area. Probe densities in the NanoBioArray channel were used in the model as the θ_0 values. They also were compared to the probe densities on the SPR sensors, as estimated using the level of SPR signal enhancement that occurred following immobilization. The hybridization and dehybridization constants were determined using SPR spectroscopy. COMSOL Multiphysics 3.5 software (COMSOL Group) was used to perform calculations to simulate θ^{pm} and θ^{mm} at specific time points during the experiment.

DNA Probe Immobilization and DNA Target Hybridization in a NanoBioArray Chip. The use of the NanoBioArray chip has been previously reported.[53−55] Briefly, the NanoBioArray chip comprises of a PDMS slab (2 in. × 2 in.) with 16 straight microchannels, sealed reversibly to a microscope glass slide. The width of straight channels was 200 μm, and the height was 35 μm.

The probe immobilization procedure was similar to that used by previously reported studies.[53,55] Briefly, 0.5 μL of probe solution (in 1.0 M NaCl + 0.15 M $NaHCO_3$) was added to the NanoBioArray chip, and a vacuum was applied at the outlet reservoir to fill the channels. The probe solution was pumped out of the channel after 30 min of incubation at room temperature. Subsequent to washing of the channel, the PDMS slab was peeled off, leaving behind 16 probe lines printed on the glass slide, which was then rinsed and dried. Another PDMS slab with 16 channels was sealed against the glass slide with the preprinted probe lines to carry out the DNA hybridization. These straight channels were prepared in an orthogonal direction to the array of parallel probe lines printed onto the surfaces of the glass slides.

Before introduction to the channel reservoirs, target oligonucleotides were conjugated with the AuNPs (AuNP target). In order to achieve this, the AuNP solution was added to the target solution and the mixture was incubated at 95 °C for 5 min. As DNA loading on the AuNP surfaces should make the particles stable against salt-induced aggregation,[10,11] no aggregates were observed upon successful DNA loading, as confirmed calorimetrically and also by analysis using transmission electron microscopy (TEM) of salt-stabilized AuNPs in the presence of target strands (Figure S3, Supporting Information). For TEM imaging 10 μL aliquots of this solution was drop cast onto a copper TEM grid coated with carbon and Formvar (300 mesh; Electron Microscopy Sciences, Hatfield, PA, USA) and dried under vacuum in a desiccator. These particles were imaged using a TEM (H-8100, Hitachi) operating at 200 kV. The control solutions (pristine AuNPs in aqueous and hybridization buffer solutions) were prepared for TEM imaging using similar methods to those for the AuNP target solutions except that they were not mixed with the target molecules.

The AuNP target solution (0.5 μL), prepared in hybridization buffer (1× SSC + 0.2% SDS) with a final concentration of 10 nM, was added to the inlet reservoir and then filled in the channel using vacuum suction. The hybridization of the targets to the complementary probes occurred at the intersection of target channels with the probe lines, resulting in hybridization patches of 200 μm × 200 μm in dimensions. The target solutions were pumped out from the channels after incubation time of 20 min (unless noted otherwise) at room temperature (22 °C). High-temperature experiments were achieved by heating the NanoBioArray chip using a Peltier device.

After washing the channel, a solution containing streptavidin-Cy5 (50 μg/mL in 1× PBS buffer) was added to the channels and incubated for 15 min, the channel was rinsed using a wash solution (1× PBS, Tween-20 0.1%) and the PDMS slab was peeled away from the glass slide. The fluorescence detection was carried out by imaging the glass slide with a confocal laser fluorescent scanner (Typhoon 9410, GE Healthcare) at 10-μm resolution, as previously described.[56,57] The excitation and emission wavelengths were 633 and 670 nm, respectively.

The photomultiplier tube voltage was set to 600 V. The scanned image was analyzed by IMAGEQUANT 5.2 software.

Conflict of Interest: The authors declare no competing financial interest.

Acknowledgment. We gratefully acknowledge financial support from the Natural Sciences and Engineering Research Council of Canada for a Discovery Grant, and the Canada Research Chairs Program (B.D. Gates). We are thankful to Lin Wang for initial experiments and simulations, Dr. Dipankar Sen for useful advice and technical support as well as Dr. Naveed Gulzar for assistance in the SPR measurements. This work made use of 4D LABS shared facilities supported by the Canada Foundation for Innovation (CFI), British Columbia Knowledge Development Fund (BCKDF), Western Economic Diversification Canada, and SFU.

Supporting Information Available: Figure S1: The SPR sensograms resulting from kinetic titration analysis. Figure S2: The results of data analyses performed to test the impact of free targets on the measured rate constants. Figure S3: Transmission electron microscopy (TEM) images of AuNPs before and after loading with target oligonucleotides. Table S1: Details of the sequences for oligonucleotides used in this study. Table S2: calculations of the activation enthalpy and entropy with rate constants derived from Arrhenius plots. This material is available free of charge *via* the Internet at http://pubs.acs.org.

Note Added after ASAP Publication: This paper was published ASAP on July 1, 2014. A correction was made to eq 9 and the revised version was reposted on July 22, 2014.

REFERENCES AND NOTES

1. Elghanian, R.; Storhoff, J. J.; Mucic, R. C.; Letsinger, R. L.; Mirkin, C. A. Selective Colorimetric Detection of Polynucleotides Based on the Distance-Dependent Optical Properties of Gold Nanoparticles. *Science* **1997**, *277*, 1078–1081.
2. Rosi, N. L.; Mirkin, C. A. Nanostructures in Biodiagnostics. *Chem. Rev.* **2005**, *105*, 1547–1562.
3. Taton, T. A.; Mirkin, C. A.; Letsinger, R. L. Scanometric DNA Array Detection with Nanoparticle Probes. *Science* **2000**, *289*, 1757–1760.
4. Park, S.-J.; Taton, T. A.; Mirkin, C. A. Array-Based Electrical Detection of DNA with Nanoparticle Probes. *Science* **2002**, *295*, 1503–1506.
5. Zhao, X.; Tapec-Dytioco, R.; Tan, W. Ultrasensitive DNA Detection Using Highly Fluorescent Bioconjugated Nanoparticles. *J. Am. Chem. Soc.* **2003**, *125*, 11474–11475.
6. Tiwari, P. M.; Vig, K.; Dennis, V. A.; Singh, S. Functionalized Gold Nanoparticles and Their Biomedical Applications. *Nanomaterials* **2011**, *1*, 31–63.
7. Cheng, Y.; Stakenborg, T.; Dorpe, P.; Lagae, L.; Wang, M.; Chen, H.; Borghs, G. Fluorescence Near Gold Nanoparticles for DNA Sensing. *Anal. Chem.* **2011**, *83*, 1307–1314.
8. Daniel, M. C.; Didier, A. Gold Nanoparticles: Assembly, Supramolecular Chemistry, Quantum-Size-Related Properties, and Applications toward Biology, Catalysis, and Nanotechnology. *Chem. Rev.* **2004**, *104*, 293–346.
9. Prasad, B. L. V.; Sorensen, C. M.; Klabunde, K. J. Gold Nanoparticle Superlattices. *Chem. Soc. Rev.* **2008**, *37*, 1871–1883.
10. Li, H.; Rothberg, L. J. Colorimetric Detection of DNA Sequences Based on Electrostatic Interactions with Unmodified Gold Nanoparticles. *Proc. Natl. Acad. Sci. U. S. A.* **2004**, *101*, 14036–14039.
11. Li, H.; Rothberg, L. J. Label-Free Colorimetric Detection of Specific Sequences in Genomic DNA Amplified by the Polymerase Chain Reaction. *J. Am. Chem. Soc.* **2004**, *126*, 10958–10961.
12. Nelson, E. M.; Rothberg, L. J. Kinetics and Mechanism of Single-Stranded DNA Adsorption onto Citrate-Stabilized Gold Nanoparticles in Colloidal Solution. *Langmuir* **2011**, *27*, 1770–1777.
13. Zhang, X.; Servos, M. R.; Liu, J. Surface Science of DNA Adsorption onto Citrate-Capped Gold Nanoparticles. *Langmuir* **2012**, *28*, 3896–3902.
14. Liu, J. Adsorption of DNA onto Gold Nanoparticles and Graphene Oxide: Surface Science and Applications. *Phys. Chem. Chem. Phys.* **2012**, *14*, 10485–10496.
15. Lee, H.; Joo, S. W.; Lee, S. Y.; Lee, C. H.; Yoon, K. A.; Lee, K. Colorimetric Genotyping of Single Nucleotide Polymorphism Based on Selective Aggregation of Unmodified Gold Nanoparticles. *Biosens. Bioelectron.* **2010**, *26*, 730–735.
16. Ray, P. C.; Darbha, G. K.; Ray, A. A Gold-Nanoparticle-Based Fluorescence Resonance Energy Transfer Probe for Multiplexed Hybridization Detection: Accurate Identification of Bio-Agents DNA. *Nanotechnology* **2007**, *18*, 375504.
17. Tan, Y. N.; Lee, K. H.; Su, X. Study of Single-Stranded DNA Binding Protein−Nucleic Acids Interactions using Unmodified Gold Nanoparticles and Its Application for Detection of Single Nucleotide Polymorphisms. *Anal. Chem.* **2011**, *83*, 4251–4257.
18. Ray, P. C. Diagnostics of Single Base-Mismatch DNA Hybridization on Gold Nanoparticles by Using the Hyper-Rayleigh Scattering Technique. *Angew. Chem., Int. Ed.* **2006**, *45*, 1151–1154.
19. Liang, A.; Ouyang, H.; Jiang, Z. Resonance Scattering Spectral Detection of Trace ATP Based on Label-Free Aptamer Reaction and Nanogold Catalysis. *Analyst* **2011**, *136*, 4514–4519.
20. Li, H.; Liang, R.; Turner, D. H.; Rothberg, L. J.; Duan, S. Selective Quenching of Fluorescence from Unbound Oligonucleotides by Gold Nanoparticles As a Probe of RNA Structure. *RNA* **2007**, *13*, 2034–2041.
21. Wang, J.; Wang, L.; Liu, X.; Liang, Z.; Song, S.; Li, W.; Li, G.; Fan, C. A Gold Nanoparticle-Based Aptamer Target Binding Readout for ATP Assay. *Adv. Mater.* **2007**, *19*, 3943–3946.
22. Derbyshire, N.; White, S. J.; Bunka, D. H. J; Song, L.; Stead, S.; Tarbin, J.; Sharman, M.; Zhuo, D.; Stockley, P. G. Toggled RNA Aptamers Against Aminoglycosides Allowing Facile Detection of Antibiotics Using Gold Nanoparticle Assays. *Anal. Chem.* **2012**, *84*, 6595–6602.
23. Wang, Z.; Tang, L.; Tan, L. H.; Lu, Y. Discovery of the DNA "Genetic Code" for Abiological Gold Nanoparticle Morphologies. *Angew. Chem., Int. Ed.* **2012**, *51*, 9078–9082.
24. Wang, L.; Li, P. C. H. Gold Nanoparticle-Assisted Single Base-Pair Mismatch Discrimination on a Microfluidic Microarray Device. *Biomicrofluidics* **2010**, *4*, 032209.
25. Sedighi, A.; Li, P. C. H. Kras Gene Codon 12 Mutation Detection Enabled by Gold Nanoparticles Conducted in a NanoBioArray Chip. *Anal. Biochem.* **2014**, *448*, 58–64.
26. Wu, Y.; Liu, L.; Liang, Z.; Shen, Z.; Zhu, X. Colorimetric and Electrochemical Study on the Interaction Between Gold Nanoparticles and Unmodified DNA. *Curr. Nanosci.* **2011**, *7*, 359.
27. Cho, K.; Lee, Y.; Lee, C.-H.; Lee, K.; Kim, Y.; Choi, H.; Joo, S. W. Selective Aggregation Mechanism of Unmodified Gold Nanoparticles in Detection of Single Nucleotide Polymorphism. *J. Phys. Chem. C* **2008**, *112*, 8629.
28. Yang, J.; Lee, J. Y.; Too, H.-P.; Chow, G. M.; Gan, L. M. Single Stranded DNA Stabilization and Assembly of Au Nanoparticles of Different Sizes. *Chem. Phys.* **2006**, *323*, 304–312.
29. Yang, J.; Pong, B.-K.; Lee, J. Y.; Too, H. P. Dissociation of Double-Stranded DNA by Small Metal Nanoparticles. *J. Inorg. Biochem.* **2007**, *101*, 824–830.
30. Kimura-Suda, H.; Petrovykh, D. Y.; Tarlov, M. J.; Whitman, L. J. Base-Dependent Competitive Adsorption of Single-Stranded DNA on Gold. *J. Am. Chem. Soc.* **2003**, *125*, 9014–9015.
31. Sandstrom, P.; Boncheva, M.; Akerman, B. Nonspecific and Thiol-Specific Binding of DNA to Gold Nanoparticles. *Langmuir* **2003**, *19*, 7537–7543.
32. Sandstrom, P.; Akerman, B. Electrophoretic Properties of DNA-Modified Colloidal Gold Nanoparticles. *Langmuir* **2004**, *20*, 4182–4186.
33. Chen, C.; Wang, W.; Ge, J.; Zhao, X. S. Kinetics and Thermodynamics of DNA Hybridization on Gold Nanoparticles. *Nucleic Acids Res.* **2009**, *37*, 3756–3765.

34. Karlsson, R.; Katsamba, P. S.; Nordin, H.; Pol, E.; Myszka, D. G. Analyzing a Kinetic Titration Series Using Affinity Biosensors. *Anal. Biochem.* **2006**, *349*, 136–147.
35. Sedighi, A.; Li, P. C. H. Kinetic and Thermodynamic Analyses of DNA Hybridization reveal the Mechanism of Gold Nanoparticle-Assisted Single Base-Pair Discrimination in the Nanobioarray Chip. *MicroTAS* **2013**, 865–867.
36. Gotoh, M.; Hasegawa, Y.; Shinohara, Y.; Shimizu, M.; Tosu, M. A New Approach to Determine the Effect of Mismatches on Kinetic Parameters in DNA Hybridization Using an Optical Biosensor. *DNA Research* **1995**, *2*, 285–293.
37. Laidler, K. J. *Chemical Kinetics*, 3rd ed.; Harper and Row Publishers: New York, 1987.
38. Porschke, D.; Eigen, M. Co-Operative Non-Enzymatic Base Recognition III. Kinetics of the Helix—Coil Transition of the Oligoribouridylic−Oligoriboadenylic Acid System and of Oligoriboadenylic Acid Alone At Acidic PH. *J. Mol. Biol.* **1971**, *62*, 361–381.
39. Craig, M. E.; Crothers, D. M.; Doty, P. Relaxation Kinetics of Dimer Formation by Self Complementary Oligonucleotides. *J. Mol. Biol.* **1971**, *62*, 383–401.
40. Chu, Y. G.; Tinoco, I. J. Temperature-Jump Kinetics of the dC-G-T-G-A-A-T-T-C-G-C-G Double Helix Containing a G−T Base Pair and the dC-G-C-A-G-A-A-T-T-C-G-C-G Double Helix Containing An Extra Adenine. *Biopolymers* **1983**, *22*, 1235–1246.
41. SantaLucia, J.; Hicks, D. The Thermodynamics of DNA Structural Motifs. *Annu. Rev. Biophys. Biomol. Struct.* **2004**, *33*, 415–440.
42. Kearns, D. R. NMR Studies of Conformational States and Dynamics of DNA. *CRC Crit. Rev. Biochem.* **1984**, *15*, 237–290.
43. Ikuta, S.; Takagi, K.; Bruce, R.; Itakura, K. Dissociation Kinetics of 19 Base Paired Oligonucleotide-DNA Duplexes Containing Different Single Mismatched Base Pairs. *Nucleic Acids Res.* **1987**, *15*, 797–811.
44. Choi, C. H.; Kalosakas, G.; Rasmussen, K. O.; Hiromura, M.; Bishop, A. R.; Usheva, A. DNA Dynamically Directs Its Own Transcription Initiation. *Nucleic Acids Res.* **2004**, *32*, 1584–1590.
45. Wang, W. J.; Chen, C. L.; Qian, M. X.; Zhao, X. S. Aptamer Biosensor for Protein Detection Using Gold Nanoparticles. *Anal. Biochem.* **2008**, *373*, 213–219.
46. Okahata, Y.; Kawase, M.; Niikura, K.; Ohtake, F.; Furusawa, H.; Ebara, Y. Kinetic Measurements of DNA Hybridization on an Oligonucleotide-Immobilized 27-MHz Quartz Crystal Microbalance. *Anal. Chem.* **1998**, *70*, 1288–1296.
47. Chen, C.; Wang, W.; Wang, Z.; Wei, F.; Zhao, X. S. Influence of Secondary Structure on Kinetics and Reaction Mechanism of DNA Hybridization. *Nucleic Acids Res.* **2007**, *35*, 2875–2884.
48. Nagata, K.; Handa, H. *Real-Time Analysis of Biomolecular Interactions: Applications of BIACORE*; Springer: New York, 2000.
49. Peterson, A. W.; Heaton, R. J.; Georgiadis, R. M. The Effect of Surface Probe Density on DNA Hybridization. *Nucleic Acids Res.* **2001**, *29*, 5163–5168.
50. Löfås, S.; Mcwhirter, A. *The Art of Immobilization for SPR Sensors*. In Surface Plasmon Resonance Based Sensors, Homola, J., Ed.; Vol. 4, Springer: Berlin, 2006.
51. Berne, Bruce J.; Pecora, R. Dynamic Light Scattering: with Applications to Chemistry, Biology, and Physics. Courier Dover Publications: New York, 2000.
52. Stellwagen, E.; Lu, Y. J.; Stellwagen, N. C. Unified Description of Electrophoresis and Diffusion for DNA and Other Polyions. *Biochemistry* **2003**, *42*, 11745–11750.
53. Wang, L.; Li, P. C. H. Flexible Microarray Construction and Fast DNA Hybridization Conducted on a Microfluidic Chip for Greenhouse Plant Fungal Pathogen Detection. *J. Agric. Food Chem.* **2007**, *55*, 10509–10516.
54. Urakawa, H.; El Fantroussi, S.; Smidt, H.; Smoot, J. C.; Tribou, E. H.; Kelly, J. J.; Noble, P. A.; Stahl, D. A. Optimization of Single-Base-Pair Mismatch Discrimination in Oligonucleotide Microarrays. *Appl. Environ. Microbiol.* **2003**, *69*, 2848–2856.
55. Wang, L.; Li, P. C. H.; Yu, H. Z.; Parameswaran, M. Fungal Pathogenic Nucleic Acid Detection Achieved with a Microfluidic Microarray Device. *Anal. Chim. Acta* **2008**, *610*, 97–104.
56. Chen, H.; Wang, L.; Li, P. C. H. Nucleic Acid Microarrays Created in the Double-Spiral Format on a Circular Microfluidic Disk. *Lab Chip* **2008**, 826–829.
57. Peng, X. Y.; Li, P. C. H.; Yu, H. Z.; Parameswaran, M.; Chou, W. L. Spiral Microchannels on a CD for DNA Hybridizations. *Sens. Actuators, B* **2007**, *128*, 64–69.